Iron telluride ladder compounds: Predicting the structural and magnetic properties of $BaFe_2Te_3$

Yang Zhang,[1,2] Ling-Fang Lin,[1,2] Adriana Moreo,[1,3] Shuai Dong,[2] and Elbio Dagotto[1,3,*]
[1]*Department of Physics and Astronomy, University of Tennessee, Knoxville, Tennessee 37996, USA*
[2]*School of Physics, Southeast University, Nanjing 211189, China*
[3]*Materials Science and Technology Division, Oak Ridge National Laboratory, Oak Ridge, Tennessee 37831, USA*

(Received 12 December 2019; revised manuscript received 18 March 2020; accepted 20 March 2020; published 13 April 2020)

Since the discovery of pressure-induced superconductivity in the two-leg ladder system $BaFe_2X_3$ (X = S, Se), with the $3d$ iron electronic density $n = 6$, quasi-one-dimensional iron-based ladders have attracted considerable attention. Here, we use density-functional theory to predict that the novel $n = 6$ iron ladder $BaFe_2Te_3$ could be stable with a similar crystal structure as $BaFe_2Se_3$. Our results also indicate that $BaFe_2Te_3$ will display a complex 2×2 block-type magnetic order. Due to the magnetic striction effects of this block order, $BaFe_2Te_3$ should be a magnetic noncollinear ferrielectric system with a net polarization 0.31 $\mu C/cm^2$. In general, the similar electronic density and magnetic ground state of Te- and Se-based ladders indicates both should display similar properties. In particular, the physical and structural similarity with $BaFe_2Se_3$ suggests that $BaFe_2Te_3$ could become superconducting under high pressure.

DOI: 10.1103/PhysRevB.101.144417

I. INTRODUCTION

Since the initial discovery of superconductivity in fluorine-doped two-dimensional (2D) iron square lattices LaFeAsO, iron-based compounds have rapidly developed into one of the most important branches of unconventional superconductors in condensed-matter physics and materials science [1–4]. In the nonsuperconducting parent compounds, their magnetic ground state is known as collinear stripe order, i.e., the so-called C-type antiferromagnetic (AFM) order, with some exceptions such as block types and bicollinear types [3–6]. Since most superconducting phases always emerge next to the suppression of antiferromagnetism by carrier doping or pressure, the AFM order and AFM spin fluctuations are considered to be important for superconductivity [7,8].

Recently, pressure-induced superconductivity was observed in the two-leg quasi-one-dimensional ladder system $BaFe_2X_3$ (X = S, Se) with electronic density $n = 6.0$ [9,10], researching high-temperature iron-based superconductors [11–21]. $BaFe_2S_3$ displays a stripe-type (CX) AFM order, similar to other 2D iron-based superconductors, below 120 K [9,15]. By applying hydrostatic pressure, this system displayed an insulator-metal transition [16,22] and superconductivity was observed at $P \sim 11$ GPa near a first-order magnetic phase transition where the AFM order was suppressed [9,23]. These recent developments in the context of two-leg iron ladders remind us of the previous results for copper ladders where superconducting tendencies upon doping were theoretically predicated and later confirmed experimentally [24–26]. In fact, in iron ladders, similar pairing tendencies were observed upon hole doping by theoretical research based on density-matrix renormalization group (DMRG) at intermediate Hubbard coupling strengths [13,17]. Another possible explanation of superconductivity relies on bandwidth controlled by pressure [9].

$BaFe_2Se_3$ also shows pressure-induced superconductivity [10,20], but in addition it displays an exotic 2×2 block-type magnetic order below 256 K under ambient conditions [27]. Due to its enhanced degree of electronic correlation [28,29], the physical properties of $BaFe_2Se_3$ become more complex. For example, the existence of an orbital-selective Mott phase (OSMP) was found by neutron experiments at ambient pressure [30]. This OSMP of $BaFe_2Se_3$ was theoretically discussed based on DMRG methods by using multiorbital Hubbard models as well [31–33]. However, an additional striking experimental discovery was recently reported for this interesting material: The existence of a polar state with possible polar orbital ordering was confirmed by neutron diffraction methods combined with optical second-harmonic-generation signals [34]. In fact, this material was first theoretically predicted to be multiferroic because the block-type magnetic order can produce displacements of Se inducing broken inversion symmetry [35]. It should be noted that $BaFe_2Se_3$ is the first reported iron-based system to become both superconductor and multiferroic. Moreover, the polar state of $BaFe_2Se_3$ is an exotic noncollinear ferrielectric (FiE) phase instead of a plain ferroelectric (FE) one [34,35]. To our best knowledge, noncollinear FiE order was only proposed in a few compounds, such as MO_2X_2 (M = Mo/W, X = Br/Cl) [36] and strained $BiFeO_3$ [37]. It is reasonable to assume that finding this exotic 2×2 block-type magnetic order with quasi-one-dimensional ladders defines an effective feasible path to explore FiE materials. Besides, considering the similar atomic average electronic density in many iron superconductors, it is conceivable to obtain the superconducting phase in other potential $n = 6$ ladders as well.

*Corresponding author: edagotto@utk.edu

However, to our best knowledge, there is no other iron ladder reporting to display the 2×2 block-type magnetic order. According to our previous Hartree-Fock [38] and density-functional theory (DFT) calculations [21], the block type was expected to be stable in a large region of the Hund coupling J_H and Hubbard U phase diagram in $n = 6$ iron ladders. Hence, it can be reasonably assumed that the magnetic ground state of $n = 6$ Te-based iron ladders, not synthesized yet, may also display the block-type order if it can be prepared. Actually, the $n = 5.5$ iron Te-based ladder was synthesized in experiments [39] but it was recently predicted to display CX-type magnetic order [21]. Considering that the ionic radius of Rb^+ (∼1.47 Å) and Ba^{2+} (∼1.434 Å) are similar, we believe it should be possible to prepare Te-based $n = 6$ iron ladders with chemical formula $BaFe_2Te_3$.

In the present paper, we performed first-principles DFT calculations for the $BaFe_2Te_3$ system. Our theoretical results indicate that $BaFe_2Te_3$ should be stable with a similar crystal structure as $BaFe_2Se_3$. Because in the past, DFT has successfully predicted many new compounds before they were truly prepared, such as blue phosphorene [40] and phosphorus carbide [41,42], our structural prediction should be reliable. Moreover, the 2×2 block-type spin order is also predicted to be the most likely magnetic ground state in our calculations for this compound. In addition, we found that $BaFe_2Te_3$ should display noncollinear FiE order driven by the 2×2 block-type magnetic order via magnetic exchange striction. The magnetic state and electronic structure similarity with $BaFe_2Se_3$ further suggests that $BaFe_2Te_3$ could also become superconducting under high pressure.

II. METHOD

To understand the physical properties of the $BaFe_2Te_3$ system, first-principles DFT calculations were performed based on the projector-augmented wave (PAW) pseudopotentials with the Perdew-Burke-Ernzerhof (PBE) exchange functional, as implemented in the VIENNA AB INITIO SIMULATION PACKAGE code [43–46]. Since the spin-polarized PBE-GGA function is known to provide an accurate description of the iron-based 123-type two-leg ladder systems [12,16,19,20,22], in this paper we do not add an additional Hubbard U.

Due to the quasi-one-dimensional ladder structure, the magnetic coupling in-ladder should be the dominant factor affecting the energies and physical properties. Various possible (in-ladder) magnetic configurations were imposed on the iron ladders [21] [see Fig. 1(e)] to predict the magnetic properties, such as nonmagnetic (NM), ferromagnetic (FM), CX types with FM rungs and AFM legs, CY type with AFM rungs and FM legs, G type with both AFM rungs and legs, and 2×2 magnetic block types. Considering previous neutron results for two-leg iron ladders [9,27], the $(\pi, \pi, 0)$ order was adopted for the CX-AFM and block-AFM orders. The plane-wave cutoff energy was 500 eV. Since different magnetic configurations have different minimal unit cells, the mesh was appropriately modified for all the candidates to render the k-point densities approximately the same in reciprocal space (as example, 7×5×11 for the FM type). In addition, we have tested that these k-point meshes already lead to converged energies when compared with denser meshes. Both

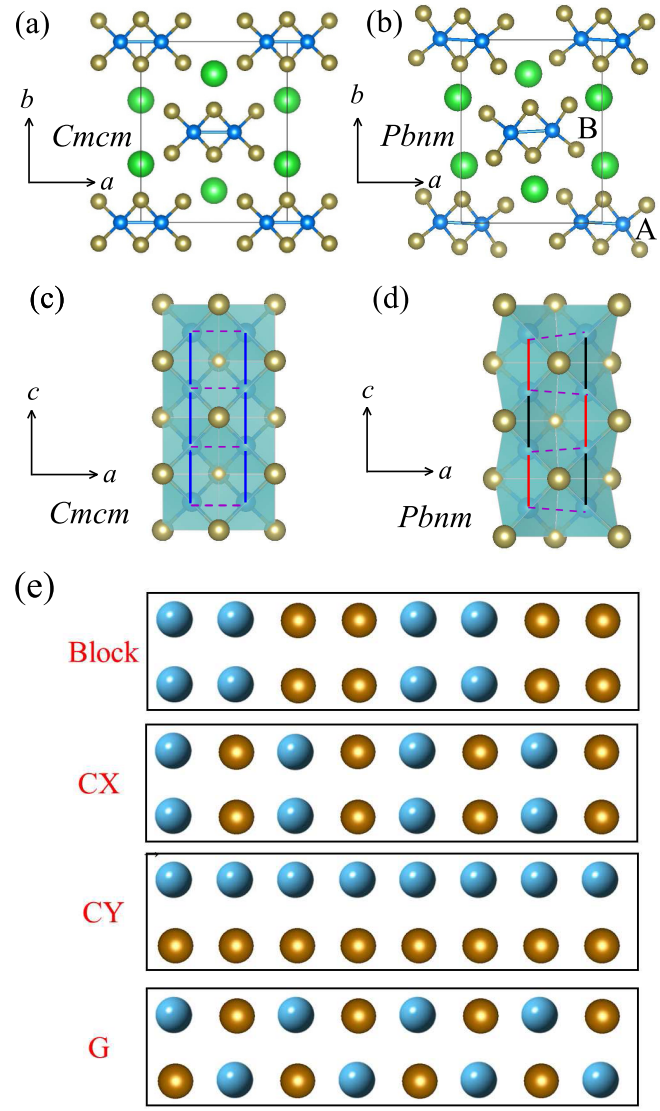

FIG. 1. (a)–(d) Schematic crystal structure of $BaFe_2Te_3$ (electronic density $n = 6$) with the conventions green = Ba, blue = Fe, dark yellow = Te. For better comparison, we used the space group *Pbnm* instead of the conventional *Pnma* since the lattice vectors of the *Pbnm* space group are the same as in the *Cmcm* space group. Note that the difference between *Pbnm* and *Pnma* space groups is only regarding the choice of a unique axis. (a), (b) Sketch of the possible crystal structures of $BaFe_2Te_3$ for the *Cmcm* (No. 63) and *Pbnm* (No. 62) phases, respectively. (c), (d) One iron ladder with highlighted $FeTe_4$ tetrahedra for the *Cmcm* and *Pbnm* phases, respectively. (e) Sketch of possible antiferromagnetic magnetic configurations in each ladder. Spin up and spin down are distinguished by different colored balls. The figure is reproduced from a previous paper [21].

the lattice constants and atomic positions were fully relaxed with different spin configurations until the Hellman-Feynman force on each atom was smaller than 0.01 eV/Å.

The phonon spectra was calculated using the finite displacement approach and analyzed by the PHONONPY software [47,48]. Furthermore, to estimate the FE polarization, the Berry phase method was adopted [49,50]. In addition

TABLE I. The optimized lattice constants (Å), local magnetic moments (in μ_B/Fe units) within the default PAW sphere, and band gaps (eV) for the various magnetic configurations using the *Cmcm* structure. Also included are the energy differences (meV/Fe) with respect to the block-B AFM configuration in the *Pbnm* phase, taken as the reference of energy. All the magnetic states discussed here were fully optimized starting from the *Cmcm* or *Pbnm* structure, respectively.

Space group	Magnetic configuration	$a/b/c$	M	Gap	Energy
Cmcm	NM	9.738/11.991/5.672	0	0	385.8
	FM	9.805/13.195/5.634	2.92	0	155.7
	CX	9.805/12.825/5.703	2.60	0	84.3
	CY	9.756/13.214/5.630	2.77	0.22	61.8
	G	9.799/12.812/5.682	2.54	0	160.7
	Block A	9.837/13.203/5.632	2.87	0.17	44.0
	Block B	9.823/13.131/5.652	2.85	0.3	24.9
Pbnm	NM	9.177/12.200/5.658	0	0	385.2
	FM	9.852/13.397/5.532	2.90	0	125.4
	CX	9.729/13.131/5.652	2.63	0.05	56.6
	CY	9.894/13.178/5.590	2.79	0.23	51.5
	G	9.840/12.852/5.643	2.46	0.06	140.3
	Block A	9.806/13.424/5.577	2.86	0.26	3.1
	Block B	9.824/13.182/5.615	2.85	0.32	0

to the standard DFT calculation discussed thus far, the maximally localized Wannier function method was employed to fit Fe 3*d*'s five bands by using the WANNIER90 packages [51].

III. RESULTS

A. Crystal structure

As shown in Fig. 1, we constructed two crystal structures [*Cmcm* (No. 63) and *Pbnm* (No. 62) phases] for $BaFe_2Te_3$, because those two types of phases were found experimentally in other 123-type iron ladders [27,52]. In the *Cmcm* phase [see Fig. 1(a)], the $FeTe_4$ tetrahedra are aligned in the *ac* plane. The *Pbnm* phase [see Fig. 1(b)] can be visualized as adding a tilting of the $FeTe_4$ tetrahedra along the *c* axis on the *Cmcm* phase of $BaFe_2Te_3$, while the two $FeTe_4$ tetrahedra along the rung direction are rotated counterclockwise/clockwise, respectively. As a consequence, as shown in Figs. 1(c)–1(d), the iron ladder would slightly distort with two different iron-iron distances along the leg direction in the *Pbnm* phase while the iron-iron distances are equal in the ideal *Cmcm* ladder. By comparing the energies of the two phases with a NM state, the *Pbnm* phase was considered to be the most likely crystal structure of $BaFe_2Te_3$ (∼1.3 meV/f.u. lower than *Cmcm* phase) after the lattice constants and atomic positions were fully relaxed. However, note that the energy difference of the two phases for the NM state are quite small and this issue will be discussed in the next section.

For completeness, starting from the crystal lattice with *Cmcm* (No. 63) and *Pbnm* (No. 62) symmetry plus various magnetic states, the different spin configurations were fully relaxed. The DFT results indicate that the crystal structure of $BaFe_2Te_3$ should be similar to $BaFe_2Se_3$ instead of $BaFe_2S_3$. In the nontilting ladder structure, all the energies of different magnetic configurations were higher than the corresponding energies of the tilting ladder structure [see Table I]. Hence, we conclude that the *Pbnm* (No. 62) phase should be the favored structure of $BaFe_2Te_3$.

B. Stability

As shown in Figs. 2(a) and 2(b), there is a small imaginary-frequency branch in the phonon spectrum of the *Cmcm* structure of $BaFe_2Te_3$, which will lead to spontaneous distortions. By removing the unstable phonon modes, the symmetry decreases from *Cmcm* to *Pbnm*. This small imaginary-frequency issue also corresponds to the small energy difference between the *Cmcm* and *Pbnm* phases. According to group theory analysis using the AMPLIMODES software [53,54], this spontaneous distortion mode is a Y^{2+} mode. For comparison, the phonon spectrum of the *Pbnm* structure of $BaFe_2Te_3$ is displayed in Figs. 2(c) and 2(d), which is dynamically stable (no unstable modes). Furthermore, we also investigated the elastic-stability conditions that indicated the *Pbnm* structure of $BaFe_2Te_3$ should be elastically stable. Moreover, based on the optimized structure for the block-B AFM magnetic order, we calculated the phonon spectrum corresponding to this magnetic state. The results indicate that this magnetic ground state is also stable, as shown in Fig. 2(e).

The elastic matrix of $BaFe_2Te_3$ has nine nonzero independent matrix elements (C_{11}, C_{12}, C_{13}, C_{22}, C_{23}, C_{33}, C_{44}, C_{55}, C_{66}) due to the *mmm* Laue class features of the *Cmcm* space group (No. 63) and *Pbnm* space group (No. 62) [55]. These values of the elastic matrix constants C_{ij}'s satisfy the Born stability criteria for an orthorhombic system [55]. We calculated the elastic matrix for both *Cmcm* and *Pbnm* phase as summarized in Table II.

TABLE II. The calculated elastic matrix elements (C_{ij}, in units of Gpa) corresponding to $BaFe_2Te_3$ for the *Cmcm* and *Pbnm* phases.

	C_{11}	C_{12}	C_{13}	C_{22}	C_{23}	C_{33}	C_{44}	C_{55}	C_{66}
No. 63	48.4	21.1	30.8	34.3	28.2	90.8	15.3	23.5	12.9
No. 62	48.8	23.7	29.1	38.8	27.4	88	15.7	23.1	13.9

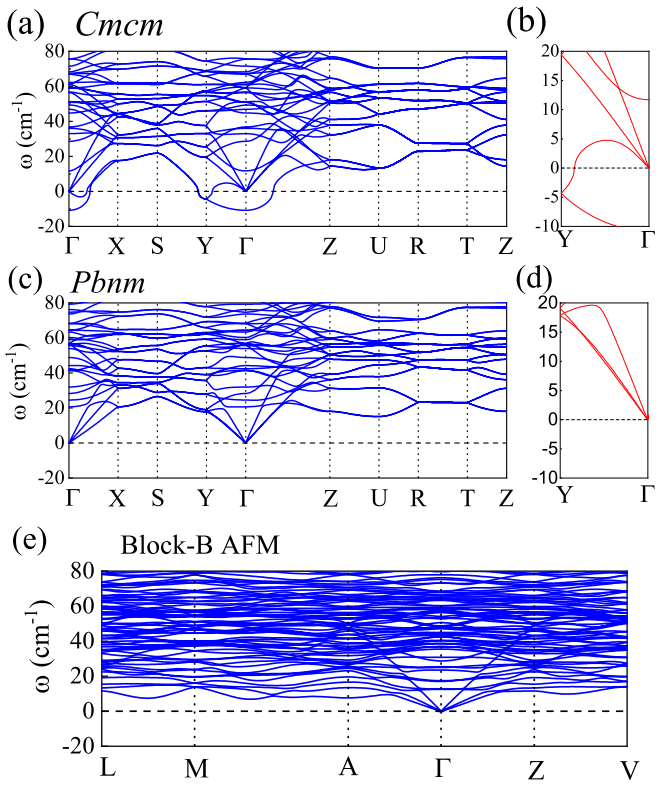

FIG. 2. (a)–(d) Phonon spectrum of $BaFe_2Te_3$ (electronic density $n = 6$) for NM state. The coordinates of the high symmetry points in the bulk Brillouin zone (BZ) are given by $\Gamma = (0, 0, 0)$, $X = (0.5, 0, 0)$, $S = (0.5, 0.5, 0)$, $Y = (0, 0.5, 0)$, $Z = (0, 0, 0.5)$, $U = (0.5, 0, 0.5)$, $R = (0.5, 0.5, 0.5)$, T (0, 0.5, 0.5). (a) Sketch of the entire BZ for the *Cmcm* phase of $BaFe_2Te_3$. (b) Phonon spectrum of the *Cmcm* phase along Y-Γ. (c) Sketch of the entire BZ for the *Pbnm* phase of $BaFe_2Te_3$. (d) Phonon spectrum of the *Pbnm* phase along Y-Γ. (e) Phonon spectrum of $BaFe_2Te_3$ (electronic density $n = 6$) for the block-B AFM state. The coordinates of the high-symmetry points BZ are given by $L = (-0.5, 0, 0.5)$, $M = (-0.5, 0.5, 0.5)$, $A = (-0.5, 0, 0)$, $\Gamma = (0, 0, 0)$, $Z = (0, -0.5, 0.5)$, $V = (0, 0, 0.5)$.

The necessary and sufficient Born criteria for an orthorhombic system are the following [55]:

(1) The matrix C is definite positive.

(2) All eigenvalues of C are positive.

(3) All the leading principal minors of C (determinants of its upper-left $k \times k$ submatrix, $1 \leqslant k \leqslant 6$) are positive.

(4)

$$C_{11} > 0, \quad C_{11}C_{22} > C_{12}^2, \tag{1}$$

$$C_{11}C_{22}C_{33} + 2C_{12}C_{13}C_{23} - C_{11}C_{23}^2 - C_{22}C_{13}^2 - C_{33}C_{12}^2 > 0, \tag{2}$$

$$C_{44} > 0, \quad C_{55} > 0, \quad C_{66} > 0, \tag{3}$$

$$C_{ii} + C_{jj} - 2C_{ij} > 0. \tag{4}$$

As a consequence, $BaFe_2Te_3$ should be elastically stable.

C. Magnetism

Previous studies of iron-based superconductors suggest that in the parent compound they all ordered magnetically.

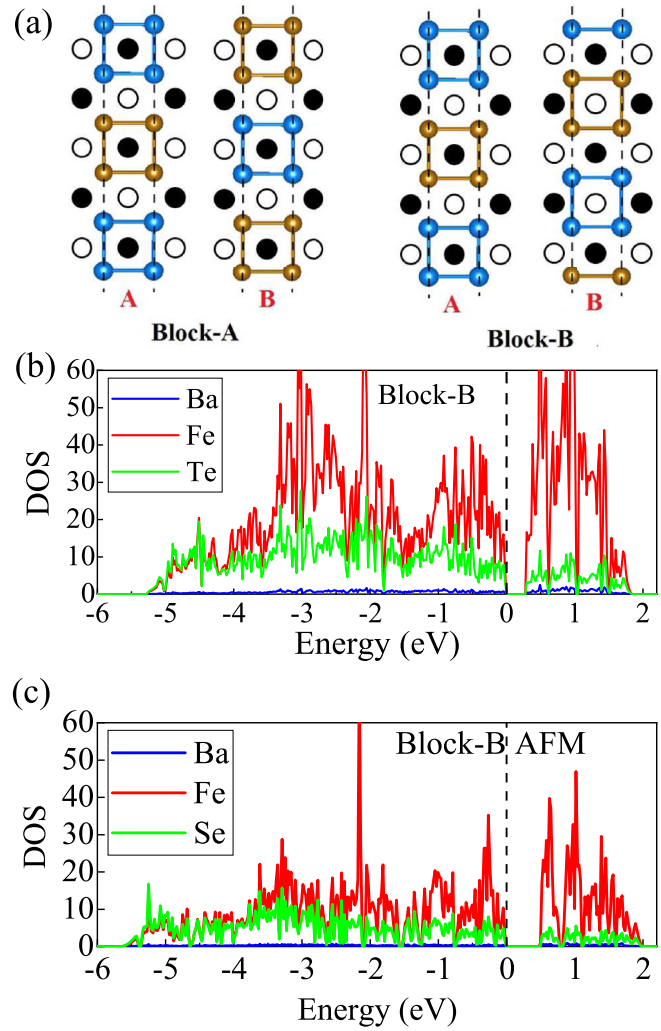

FIG. 3. (a) Sketch of block-A and block-B spin patterns studied here. Spin up and down are represented by blue and brown circles, respectively. The A and B red labels are different ladders located in different layers. The two tellurium sites denote locations above and below the iron plane defined by hollow and solid circles, respectively. (b) The density of states near the Fermi level based on the block-B states $(\pi, \pi, 0)$ for $BaFe_2Te_3$. Blue: Ba; red: Fe; green: Te. (c) The density of state near Fermi level based on the block-B states $(\pi, \pi, 0)$ for $BaFe_2Se_3$. Blue: Ba; red: Fe; green: Se.

Then, our next task is to understand the magnetic ground state of the here predicted new Te-based ladder. For this purpose, various possible (in-ladder) magnetic arrangements were tried [see Fig. 1(e)]. Considering previous neutron-based studies for $BaFe_2Se_3$ [27], the two possible block-AFM orders that were tried here are shown in Fig. 3(a). Our main results for $BaFe_2Te_3$ are summarized in Table I.

Under ambient conditions, our results indicate that the block-B AFM order is the most stable ground-state magnetic order among all the candidates considered here. For the block-B AFM state, the calculated local magnetic moment of Fe is 2.85 μ_B/Fe, quite close to the value observed experimentally and theoretically for $BaFe_2Se_3$ [20,27]. The calculated energy gap of the block-B AFM order is about 0.32 eV, which is slightly smaller than the calculated value of $BaFe_2Se_3$ [20,35].

Moreover, $BaFe_2Te_3$ could become metallic under high pressure after considering previous DFT calculations and experiments for related ladders [9,10,16,20]. A structural phase transition in the case of $BaFe_2Se_3$ was found under pressure, with the tilting ladders becoming nontilting, corresponding to a transition from the *Pbnm* symmetry to an ideal *Cmcm* symmetry [20,52]. Hence, in principle, $BaFe_2Te_3$ should also display a structural phase transition under pressure although this aspect requires further detailed calculations beyond the scope of this paper.

According to the calculated density of states (DOS) for the block-B $(\pi, \pi, 0)$ AFM order [see Fig. 3(b)], the bands near the Fermi level are primarily contributed by Fe-3*d* orbitals which are highly *hybridized* with Te-5*p* orbitals. The total bandwidth of the iron bands corresponding to the magnetic ground state of $BaFe_2Te_3$ (∼7 eV) is slightly smaller than the bandwidths of $BaFe_2S_3$ (∼8 eV) [21] and $BaFe_2Se_3$(∼7.6 eV) [56] [see Fig. 3(c)]. This suggests that the degree of electronic correlation effects of the Te-based ladders should be similar to other iron $n = 6$ ladders, although only explicit calculations of the Hubbard and Hund couplings, both important in multiorbital systems, can confirm this assumption. Because many believe that the block-type magnetic order of $BaFe_2Se_3$ is related to an orbital selective Mott state induced by electronic correlations [27,31–33], it is reasonable to conclude that $BaFe_2Te_3$ could also display this interesting state as well. Of course, more powerful many-body techniques based on multiorbital Hubbard models are required to confirm this OSMP hypothesis.

D. Ferrielectricity

Due to magnetic-exchange striction effect, the block spin configuration will break parity symmetry but will not break space-inversion symmetry in the iron ladder. However, as shown in Fig. 4(a), the displacements of the Te atoms would break space-inversion symmetry. This will induce local

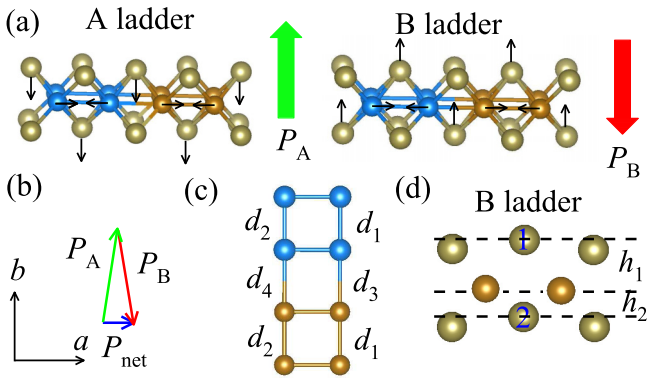

FIG. 4. (a) Sketch of the Fe-Te ladders A and B with block AFM order. Partial Te atomic displacements induced by the exchange striction effect of the Block order of Fe. (b) Vector of polarizations of the different ladders A and B, as well as the net polarization. (c) Sketch of one ladder with the optimized bock-B AFM order of $BaFe_2Te_3$, showing the NN spin up-up (or down-down) and NN spin up-down Fe-Fe distances. (d) Sketch along ladder B of the optimized block-B AFM order of $BaFe_2Te_3$. The different heights of Te are marked h_1 and h_2, respectively.

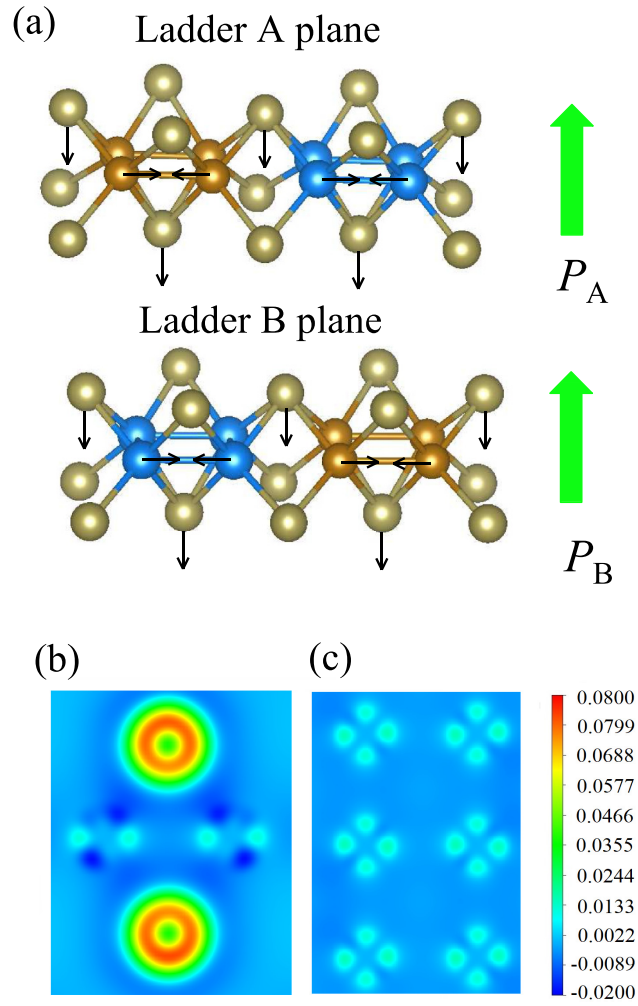

FIG. 5. (a) Sketch of Fe-Te ladder A with π-phase shift of block AFM order. Partial Te ionic displacements moved down, which is induced by the exchange striction effect of block order of Fe. (b), (c) The electronic density difference ($BaFe_2Se_3$ minus $BaFe_2Te_3$). (b) The Te-Fe-Te-Fe bonds plane. (c) The iron ladder plane.

dipoles for each iron ladder since irons would move in the same direction perpendicular to the ladder's plane. Due to the phase difference between the A and B ladders in the block-B AFM state of $BaFe_2Te_3$, the induced polarization of each ladder is, in principle, opposite. However, there will be a remaining net polarization along the *a* axis since the ladders A and B are slightly tilting, as displayed in Fig. 4(b). This conclusion is also supported by group theory analysis [57].

It should also be noticed that the π-phase shift will not change the direction of *P*. Although there is a π-phase shift in each AA/BB ladder plane for the block-A AFM $(\pi, \pi, 0)$ order, the movements of Te atoms, induced by the block order, are all in the same direction as shown in Fig. 5(a).

In our fully optimized crystal structure of block-B AFM order of $BaFe_2Te_3$, the nearest-neighbor (NN) distances of spin up-up [or down-down] Fe-Fe are $d_1 = 2.583$ Å and $d_2 = 2.594$ Å, and the NN distances of spin up-down Fe-Fe are $d_3 = 3.031$ Å and $d_2 = 3.020$ Å, as displayed in Fig. 4(c). Meanwhile, our DFT results indicate that the heights of Te(1)

and Te(2) are different: 1.987 Å and 1.454 Å, respectively, which is in agreement with our symmetry and group analysis mentioned in the previous paragraph. Those numerical results show that the FE dipole of $BaFe_2Te_3$ would be larger than the value of $BaFe_2Se_3$ by comparing the height difference of different chalcogens (for Te: $\Delta h \sim 0.53$ Å, while for Se: $\Delta h \sim 0.22$ Å [35]). The calculated P of $BaFe_2Te_3$ is about 0.31 $\mu C/cm^2$, which is larger than the value for $BaFe_2Se_3$ (0.19 $\mu C/cm^2$) [35]. The FiE polarization is directly proportional to the effective ionic charge and relative displacement from paraelectric state, and inversely proportional to volume. Although the difference in distance of the heights of Te is more than twice that of the heights of Se, the value of the polarization of $BaFe_2Te_3$ is not twice as large as that of $BaFe_2Se_3$. This is because we also have to consider that the effective ionic charge within chalcogenides decreases from Se to Te, while the volume of $BaFe_2Se_3$ is smaller than $Ba_2Fe_2Te_3$. We present the electronic density difference between $BaFe_2Se_3$ and $BaFe_2Te_3$ in Figs. 5(b) and 5(c). It is clearly shown that the Se anions with bright red spheres attract more electrons than the Te anions, while the dark blue negative electronic density difference in the iron ladder plane indicates that the Fe cations lost electrons in the case of Se as compared with the $BaFe_2Te_3$ system. Overall, this suggests that the electronegativity of Te is weaker than Se.

More importantly, because the ladders for each layer are tilted in different directions, the corresponding induced FE dipoles would correspond to a noncollinear order as shown in Fig. 4(b). Its noncollinearities may be easily modulated by external electric fields. If we only consider the exchange striction without magnetic order, the space group of our fully relaxed FiE structure is $Pnm2_1$ (No. 31), which is consistent with recent neutron experiments for $BaFe_2Se_3$ [34].

IV. ADDITIONAL DISCUSSION

In Fig. 6(a), we present the projected band structure of the fully optimized NM states for the five iron 3d orbitals corresponding to $BaFe_2Te_3$. For better understanding, we changed the lattice vectors of the *Pbnm* space group to the conventional *Pnma* space group where the b axis is along the ladder direction, the c axis is perpendicular to the ladders but still in the iron layer, and the a axis is perpendicular to the iron layer. It is clearly shown that the band structure is more dispersive along the ladder direction ($X - S$ path) than other directions, which indicates the quasi-one-dimensional ladder behavior along the k_y axis. Near the Fermi level, the bands are mainly contributed by d_{xz}, d_{yz}, and $d_{3z^2-r^2}$ [note that the cartesian axes correspond to the lattice axis of *Pnma* symmetry [28]; i.e., the x axis is a, y axis is b, and z axis is c in Fig. 1(b)]. Based on the Wannier fitting results, the bandwidth of the five iron orbitals is about 4.1 eV, as shown in Fig. 6(b). Since the crystal constants of the fully optimized NM state are usually smaller than the experimental lattice constants in iron ladder systems, the "real" noninteracting bandwidth of the five iron orbitals would be smaller than this value. To better understand the electronic correlation of $BaFe_2Te_3$ and the electronic structural similarity with $BaFe_2Se_3$, we display the electronic structure of $BaFe_2Se_3$ for the fully optimized NM phase in Fig. 7. In $BaFe_2Se_3$, the band structure is quite

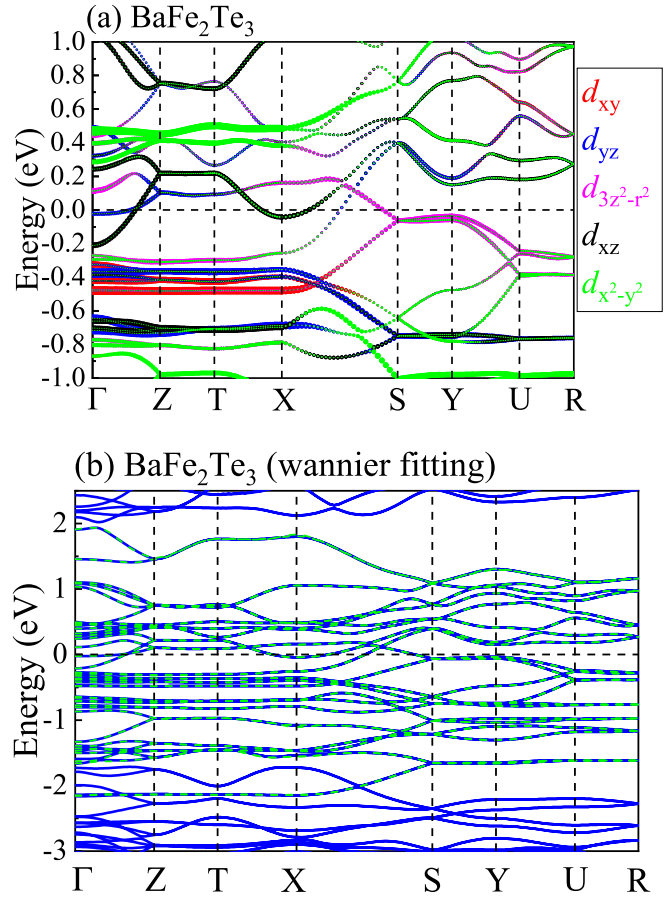

FIG. 6. (a) Projected band structures of $BaFe_2Te_3$ (electronic density $n = 6$) for the nonmagnetic (NM) state. The Fermi level is shown with dashed lines. The weight of each iron orbital is represented by the size of the circle. (b) The original band dispersion is shown by blue solid lines, while the Wannier interpolated band dispersion is shown using green dashed curves for $BaFe_2Te_3$. The coordinates of the high symmetry points in bulk BZ are given by $\Gamma = (0, 0, 0)$, $Z = (0, 0, 0.5)$, $T = (-0.5, 0, 0.5)$, $X = (-0.5\ 0\ 0)$, $S = (-0.5, 0.5, 0)$, $Y = (0, 0, 5, 0)$, $U = (0, 0.5, 0.5)$, $R = (-0.5, 0.5, 0.5)$.

similar to $BaFe_2Te_3$ because the Fermi levels are also mainly contributed by d_{xz}, d_{yz}, and $d_{3z^2-r^2}$ orbitals. As shown in Fig. 7(b), the bandwidth of the 123-Se $n = 6$ ladder for the optimized NM structure is about 4.5 eV. Considering the similar bandwidth and band structure with $BaFe_2Se_3$, it is reasonable to assume that electronic correlation effects would be as interesting in Te-based ladders as they are in Se-based ladders.

The vast majority of reported 2D iron superconductors [1–4] display a similar structural lattice, magnetic ground state, and electronic structure. Then, it is reasonable that according to our DFT results, the physical and structural properties of our predicted $BaFe_2Te_3$ are very similar to those of $BaFe_2Se_3$. The $BaFe_2S_3$ has a CX-type AFM order at ambient conditions, and the superconducting transition temperature of $BaFe_2S_3$ is higher than $BaFe_2Se_3$ (the 2×2 block-type AFM order). It suggests that $BaFe_2Te_3$ could also become superconducting under pressure although with a lower

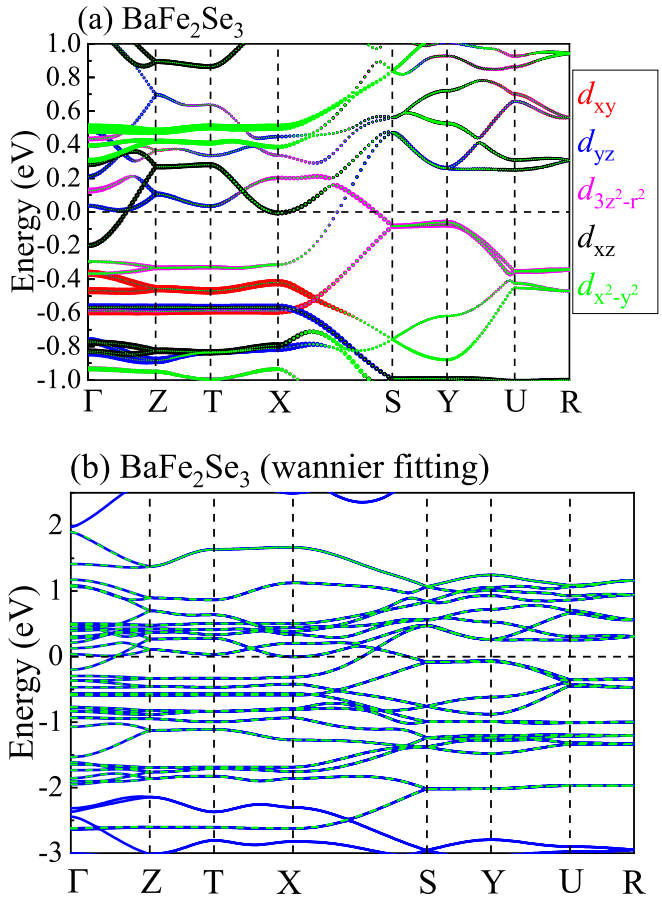

FIG. 7. (a) Projected band structures of $BaFe_2Se_3$ (electronic density $n = 6$) for the nonmagnetic (NM) state. The Fermi level is shown with dashed lines. The weight of each iron orbital is represented by the size of the circle. (b) The original band dispersion is shown by blue solid lines, while the Wannier interpolated band dispersion is shown using green dashed curves for $BaFe_2Se_3$. The coordinates of the high symmetry points in bulk BZ are given by $\Gamma = (0, 0, 0)$, $Z = (0, 0, 0.5)$, $T = (-0.5, 0, 0.5)$, $X = (-0.5\ 0\ 0)$, $S = (-0.5, 0.5, 0)$, $Y = (0, 0{,}5, 0)$, $U = (0, 0.5, 0.5)$, $R = (-0.5, 0.5, 0.5)$.

transition temperature than $BaFe_2S_3$ because our 123-Te ladder is very similar to $BaFe_2Se_3$ which has a lower critical temperature than the 123-S ladder.

Since the pressure-induced superconducting phase domes of iron ladders were found near the AFM phase [9,10], it is reasonable to assume that the driving force of superconductivity are the AFM spin fluctuations [12,20]. The block AFM order of $BaFe_2Se_3$ was considered to possibly change to the stripe CX-AFM structure due to a structural transition under pressure [10,20]. In this scenario, the magnetic fluctuations of $BaFe_2Se_3$ were considered to be induced by the competition between block- and CX-type magnetic orders, while the magnetic fluctuations of $BaFe_2S_3$ were attributed entirely to the CX-type AFM order. Hence, it is reasonable to assume that the competition between block and CX-type magnetic order would be the driving force for superconductivity in high-pressured $BaFe_2Te_3$ as well. It should also be noted that, in previous 2D iron superconductors, the d_{xy} orbital was considered to be very important to understand the transition temperature [58,59], corresponding to our d_{yz} orbital lying in the iron ladder plane. This issue deserves to be studied more in depth by powerful many-body techniques, beyond the capabilities of the DFT calculations.

V. CONCLUSION

In summary, the two-leg iron ladder compound $BaFe_2Te_3$, with the iron density $n = 6$ was systematically studied by using first-principles calculations. The block-B type AFM state is here predicted to be the most likely magnetic ground state. Considering the exotic Block order and strong correlation in this $n = 6$ iron Te ladder, the phenomenon of OSMP is expected. In addition, using the symmetry analysis and DFT calculations, the presence of noncollinear ferrieletricity in $BaFe_2Te_3$ is here predicted as induced by the magnetic exchange striction effects of the block order. Moreover, considering the magnetic state similarity and electronic structure with other iron ladders, $BaFe_2Te_3$ may become superconducting under higher pressure. Our overarching conclusion is that the $n = 6$ iron Te ladder is worth being studied by theoretical and experimental procedures because using Te could lead to interesting results, such as exotic magnetic states, an OSMP, noncollinear ferrieletricity, as well as superconductivity under high pressure.

ACKNOWLEDGMENTS

E.D. and A.M. were supported by the U.S. Department of Energy (DOE), Office of Science, Basic Energy Sciences (BES), Materials Sciences and Engineering Division. S.D., Y.Z., and L.-F.L. were supported by the National Natural Science Foundation of China (Grants No. 11834002 and No. 11674055). L.-F.L. and Y.Z. were supported by the China Scholarship Council. Y.Z. was also supported by the Scientific Research Foundation of Graduate School of Southeast University (Grant No. YBPY1826). Most calculations were carried out at the Advanced Computing Facility (ACF) of the University of Tennessee Knoxville (UTK).

[1] G. R. Stewart, Rev. Mod. Phys. **83**, 1589 (2011).
[2] D. C. Johnston, Adv. Phys. **59**, 803 (2010).
[3] E. Dagotto, Rev. Mod. Phys. **85**, 849 (2013).
[4] P. C. Dai, Rev. Mod. Phys. **87**, 855 (2015).
[5] W. Li, H. Ding, P. Deng, K. Chang, C. L. Song, K. He, L. L. Wang, X. C. Ma, J. P. Hu, X. Chen, and Q. K. Xue, Nat. Phys. **8**, 126 (2012).
[6] Y. Zhang, H. M. Zhang, Y. K. Weng, L. F. Lin, X. Y. Yao, and S. Dong, Phys. Status Solidi RRL **10**, 757 (2016).
[7] P. C. Dai, J. P. Hu, and E. Dagotto, Nat. Phys. **8**, 709 (2012).
[8] I. I. Mazin and M. D. Johannes, Nat. Phys. **5**, 141 (2009).
[9] H. Takahashi, A. Sugimoto, Y. Nambu, T. Yamauchi, Y. Hirata, T. Kawakami, M. Avdeev, K. Matsubayashi, F. Du, C.

Kawashima, H. Soeda, S. Nakano, Y. Uwatoko, Y. Ueda, T. J. Sato, and K. Ohgushi, Nat. Mater. **14**, 1008 (2015).
[10] J.-J. Ying, H. C. Lei, C. Petrovic, Y.-M. Xiao, and V.-V. Struzhkin, Phys. Rev. B **95**, 241109(R) (2017).
[11] T. Yamauchi, Y. Hirata, Y. Ueda, and K. Ohgushi, Phys. Rev. Lett. **115**, 246402 (2015).
[12] R. Arita, H. Ikeda, S. Sakai, and M.-T. Suzuki, Phys. Rev. B **92**, 054515 (2015).
[13] N. D. Patel, A. Nocera, G. Alvarez, R. Arita, A. Moreo, and E. Dagotto, Phys. Rev. B **94**, 075119 (2016).
[14] M. Wang, M. Yi, S. J. Jin, H. C. Jiang, Y. Song, H. Q. Luo, A. D. Christianson, C. de la Cruz, E. Bourret-Courchesne, D. X. Yao, D. H. Lee, and R. J. Birgeneau, Phys. Rev. B **94**, 041111(R) (2016).
[15] S. X. Chi, Y. Uwatoko, H. B. Cao, Y. Hirata, K. Hashizume, T. Aoyama, and K. Ohgushi, Phys. Rev. Lett. **117**, 047003 (2016).
[16] Y. Zhang, L. F. Lin, J. J. Zhang, E. Dagotto, and S. Dong, Phys. Rev. B **95**, 115154 (2017).
[17] N. D. Patel, A. Nocera, G. Alvarez, A. Moreo, and E. Dagotto, Phys. Rev. B **96**, 024520 (2017).
[18] J. M. Pizarro and E. Bascones, Phys. Rev. Mater. **3**, 014801 (2019).
[19] L. Zheng, B. A. Frandsen, C. Wu, M. Yi, S. Wu, Q. Huang, E. Bourret-Courchesne, G. Simutis, R. Khasanov, D.-X. Yao, M. Wang, and R. J. Birgeneau, Phys. Rev. B **98**, 180402(R) (2018).
[20] Y. Zhang, L. F. Lin, J. J. Zhang, E. Dagotto, and S. Dong, Phys. Rev. B **97**, 045119 (2018).
[21] Y. Zhang, L. F. Lin, A. Moreo, S. Dong, and E. Dagotto, Phys. Rev. B **100**, 184419 (2019).
[22] M. T. Suzuki, R. Arita, and H. Ikeda, Phys. Rev. B **92**, 085116 (2015).
[23] P. Materne, W. Bi, J. Zhao, M. Y. Hu, M. L. Amigó, S. Seiro, S. Aswartham, B. Büchner, and E. E. Alp, Phys. Rev. B **99**, 020505(R) (2019).
[24] E. Dagotto, J. Riera, and D. Scalapino, Phys. Rev. B **45**, 5744(R) (1992).
[25] E. Dagotto and T. M. Rice, Science **271**, 618 (1996); See also E. Dagotto, Rep. Prog. Phys. **62**, 1525 (1999).
[26] M. Uehara, T. Nagata, J. Akimitsu, H. Takahashi, N. Mori, and K. Kinoshita, J. Phys. Soc. Jpn. **65**, 2764 (1996).
[27] J. M. Caron, J. R. Neilson, D. C. Miller, K. Arpino, A. Llobet, and T. M. McQueen, Phys. Rev. B **85**, 180405(R) (2012).
[28] J. M. Caron, J. R. Neilson, D. C. Miller, A. Llobet, and T. M. McQueen, Phys. Rev. B **84**, 180409(R) (2011).
[29] Y. Nambu, K. Ohgushi, S. Suzuki, F. Du, M. Avdeev, Y. Uwatoko, K. Munakata, H. Fukazawa, S. X. Chi, Y. Ueda, and T. J. Sato, Phys. Rev. B **85**, 064413 (2012).
[30] M. Mourigal, S. Wu, M. B. Stone, J. R. Neilson, J. M. Caron, T. M. McQueen, and C. L. Broholm, Phys. Rev. Lett. **115**, 047401 (2015).
[31] J. Herbrych, N. Kaushal, A. Nocera, G. Alvarez, A. Moreo, and E. Dagotto, Nat. Commun. **9**, 3736 (2018).
[32] N. D. Patel, A. Nocera, G. Alvarez, A. Moreo, S. Johnston, and E. Dagotto, Commun. Phys. **2**, 64 (2019).
[33] J. Herbrych, J. Heverhagen, N. D. Patel, G. Alvarez, M. Daghofer, A. Moreo, and E. Dagotto, Phys. Rev. Lett. **123**, 027203 (2019).
[34] T. Aoyama, S. Imaizumi, T. Togashi, Y. Sato, K. Hashizume, Y. Nambu, Y. Hirata, M. Matsubara, and K. Ohgushi, Phys. Rev. B **99**, 241109(R) (2019).
[35] S. Dong, J. M. Liu, and E. Dagotto, Phys. Rev. Lett. **113**, 187204 (2014).
[36] L.-F. Lin, Y. Zhang, A. Moreo, E. Dagotto, and S. Dong, Phys. Rev. Lett. **123**, 067601 (2019).
[37] Y. Yang, J. Íñiguez, A.-J. Mao, and L. Bellaiche, Phys. Rev. Lett. **112**, 057202 (2014).
[38] Q. Luo, A. Nicholson, J. Rincón, S. Liang, J. Riera, G. Alvarez, L. Wang, W. Ku, G. D. Samolyuk, A. Moreo, and E. Dagotto, Phys. Rev. B **87**, 024404 (2013).
[39] K. O. Klepp, W. Sparlinek, and H. Boller, J. Alloys Compd. **238**, 1 (1996).
[40] J. Guan, Z. Zhu, and D. Tománek, Phys. Rev. Lett. **113**, 046804 (2014).
[41] J. Guan, D. Liu, Z. Zhu, and D. Tománek, Nano Lett. **16**, 3247 (2016).
[42] W. C. Tan, Y. Cai, R. Ng, L. Huang, X. Feng, G. Zhang, Y.-W. Zhang, C. A. Nijhuis, X. Liu, and K.-W. Ang, Adv. Mater. **29**, 1700503 (2017).
[43] G. Kresse and J. Hafner, Phys. Rev. B **47**, 558 (1993).
[44] G. Kresse and J. Furthmüller, Phys. Rev. B **54**, 11169 (1996).
[45] P. E. Blöchl, Phys. Rev. B **50**, 17953 (1994).
[46] J. P. Perdew, K. Burke, and M. Ernzerhof, Phys. Rev. Lett. **77**, 3865 (1996).
[47] L. Chaput, A. Togo, I. Tanaka, and G. Hug, Phys. Rev. B **84**, 094302 (2011).
[48] A. Togo and I. Tanaka, Scr. Mater. **108**, 1 (2015).
[49] R. D. King-Smith and D. Vanderbilt, Phys. Rev. B **47**, 1651 (1993).
[50] R. Resta, Rev. Mod. Phys. **66**, 899 (1994).
[51] A. A. Mostofi, J. R. Yates, Y. S. Lee, I. Souza, D. Vanderbilt, and N. Marzari, Phys. Commun. **178**, 685 (2007).
[52] V. Svitlyk, D. Chernyshov, E. Pomjakushina, A. Krzton-Maziopa, K. Conder, V. Pomjakushin, R. Pöttgen, and V. Dmitriev, J. Phys.: Condens. Matter **25**, 315403 (2013).
[53] D. Orobengoa, C. Capillas, M. I. Aroyo, and J. M. Perez-Mato, J. Appl. Cryst. **42**, 820 (2009).
[54] J. Perez-Mato, D. Orobengoa, and M. I. Aroyo, Acta Cryst. A **66**, 558 (2010).
[55] F. Mouhat and F.-X. Coudert, Phys. Rev. B **90**, 224104 (2014).
[56] Based on the previously optimized magnetic ground state of $BaFe_2Se_3$ [20], we calculated the DOS for the block-B AFM $(\pi, \pi, 0)$ magnetic order.
[57] Using the crystal lattice plus the block-B AFM order, the magnetic space group became *Cc* (No. 9) after fully relaxing the structure. The corresponding point group of the fully relaxed block-B AFM state is *m*. A nonzero polarization *P* is allowed in this polar point group.
[58] P. J. Hirschfeld, M. M. Korshunov, and I. I. Mazin, Rep. Prog. Phys. **74**, 124508 (2011).
[59] D. J. Scalapino, Rev. Mod. Phys. **84**, 1383 (2012).